DOI:
10.1158/0008-5472.CAN-18-0759

Document Version
Peer reviewed version

Published OnlineFirst July 27, 2018; DOI: 10.1158/0008-5472.CAN-18-0759

Translational Science

Cancer Research

Metabolic Imaging Detects Low Levels of Glycolytic Activity That Vary with Levels of c-Myc Expression in Patient-Derived Xenograft Models of Glioblastoma

Richard Mair[1,2,3], Alan J. Wright[1,3], Susana Ros[1,3], De-en Hu[1,3], Tom Booth[1,3], Felix Kreis[1,3], Jyotsna Rao[1], Colin Watts[2,3], and Kevin M. Brindle[1,3,4]

Abstract

^{13}C MRI of hyperpolarized [1-^{13}C]pyruvate metabolism has been used in oncology to detect disease, investigate disease progression, and monitor response to treatment with a view to guiding treatment in individual patients. This technique has translated to the clinic with initial studies in prostate cancer. Here, we use the technique to investigate its potential uses in patients with glioblastoma (GB). We assessed the metabolism of hyperpolarized [1-^{13}C]pyruvate in an orthotopically implanted cell line model (U87) of GB and in patient-derived tumors, where these were produced by orthotopic implantation of cells derived from different patients. Lactate labeling was higher in the U87 tumor when compared with patient-derived tumors, which displayed intertumoral heterogeneity, reflecting the intra- and intertumoral heterogeneity in the patients' tumors from which they were derived. Labeling in some patient-derived tumors could be observed before their appearance in morphologic images, whereas in other tumors it was not significantly greater than the surrounding brain. Increased lactate labeling in tumors correlated with c-Myc–driven expression of hexokinase 2, lactate dehydrogenase A, and the monocarboxylate transporters and was accompanied by increased radioresistance. Because c-Myc expression correlates with glioma grade, this study demonstrates that imaging with hyperpolarized [1-^{13}C]pyruvate could be used clinically with patients with GB to determine disease prognosis, to detect early responses to drugs that modulate c-Myc expression, and to select tumors, and regions of tumors for increased radiotherapy dose.

Significance: Metabolic imaging with hyperpolarized [1-^{13}C]pyruvate detects low levels of c-Myc–driven glycolysis in patient-derived glioblastoma models, which, when translated to the clinic, could be used to detect occult disease, determine disease prognosis, and target radiotherapy. *Cancer Res; 78(18); 5408–18. ©2018 AACR.*

Introduction

Gliomas represent 80% of primary tumors affecting the adult human central nervous system and are classified into four types. The most aggressive, grade 4 glioblastoma (GB), accounts for more than 50% of all diagnosed adult gliomas (1, 2). Debulking surgery followed by radiotherapy with concomitant administration of temozolomide is the current standard of care treatment (3); however, median survival is only 15 months (4). The tumor is driven by multiple genetic alterations, including loss of the *PTEN* gene, amplification of EGFR, and increased signaling via the PI3K/Akt pathway (2, 5). The latter pathway is activated in more than 88% of cases, which results in upregulated glucose transporter expression and increased glycolysis and is associated with tumor progression and resistance to treatment (6, 7). Expression of the transcription factor c-Myc is correlated with glioma grade, and between 60% and 80% of GB exhibit elevated levels of Myc (8, 9). Myc also drives increased expression of the glycolytic enzymes to meet the elevated biosynthetic demands of increased cell proliferation (10).

Hyperpolarization of ^{13}C-labeled metabolites, which can increase their sensitivity to magnetic resonance detection by more than 10,000× (11), has revolutionized our capability to image metabolism *in vivo* (12) and has already translated to the clinic (13). Previous ^{13}C magnetic resonance spectroscopic imaging studies of hyperpolarized [1-^{13}C]pyruvate metabolism in orthotopically implanted cell line models of GB have shown much higher levels of labeled lactate in the tumor when compared with surrounding normal brain tissue (14). The purpose of this study was to determine whether this was also the case in patient-derived orthotopically implanted

[1]Cancer Research UK Cambridge Institute, University of Cambridge, Cambridge, United Kingdom. [2]Division of Neurosurgery, Department of Clinical Neurosciences, University of Cambridge, Cambridge, United Kingdom. [3]Cancer Research UK Major Centre - Cambridge, Cancer Research UK Cambridge Institute, Cambridge, United Kingdom. [4]Department of Biochemistry, University of Cambridge, Cambridge United Kingdom.

Note: Supplementary data for this article are available at Cancer Research Online (http://cancerres.aacrjournals.org/).

Current address of Colin Watts: University of Birmingham, Institute of Cancer and Genomic Sciences, Birmingham, United Kingdom.

Corresponding Author: Kevin M. Brindle, University of Cambridge, Li Ka Shing Centre, Cambridge CB2 0RE, United Kingdom. Phone: 4412-2376-9647; Fax: 4412-2376-9510; E-mail: kmb1001@cam.ac.uk

doi: 10.1158/0008-5472.CAN-18-0759

Published OnlineFirst July 27, 2018; DOI: 10.1158/0008-5472.CAN-18-0759

xenograft (PDOX) models of GB, which more faithfully reproduce the biology of patient tumors than the cell line models (15, 16), and to determine whether there were differences in pyruvate metabolism between PDOX models derived from different patients.

Materials and Methods

Assessment of intratumoral heterogeneity in patient tumors by fluorescence-guided multiregion sampling

Intraoperative sampling of 4 patients with confirmed GB was performed by an experienced neurosurgeon (C. Watts). Cytoreductive surgery was guided by giving the patients 5-aminolevulinic acid (5-ALA) 6 hours prior to surgery (17). Tissue sampling was performed using a Zeiss OPMI Pentero operating microscope (Zeiss) for fluorescence detection of protoporphyrin IX (a 5-ALA metabolite; ref. 18). Written informed consent was obtained from the patients; the studies were conducted in accordance with the Declaration of Helsinki, and were approved by an Institutional Review Board.

Cell culture

Brain tumor tissue was collected from patients with GB using protocols compliant with the UK Human Tissue Act 2004 (HTA licence ref. 12315), approved by the Local Regional Ethics Committee (LREC ref. 04/Q0108/60) and in accordance with the Declaration of Helsinki. Informed consent was obtained from each patient. Tumor tissue was disaggregated in PBS and cells isolated by filtration through a 40-μm filter (Falcon) and washed with 10 mL red blood cell lysis buffer (Abcam). Cell viability was assessed by Trypan blue dye exclusion and viable cells were seeded at 15,000 cells cm^2 and grown as monolayer cultures on extracellular matrix (ECM)-coated T_{75} flasks (Engelbreth-Holm-Swarm murine sarcoma ECM gel–1:10 dilution, Sigma-Aldrich) in phenol red-free Neurobasal A (Gibco) medium containing 20 mmol/L L-glutamine (Sigma-Aldrich), 1% streptomycin/penicillin/amphotericin B (Invitrogen), 20 ng/mL hEGF (Sigma-Aldrich), 20 ng/mL hFGF (R&D Systems), 2% B-27 (Invitrogen), and 1% N-2 (Invitrogen). U87 cells (ATCC) were grown in DMEM supplemented with 2 mmol/L L-glutamine and 10% FBS (Gibco). Cell line authentication was performed using STR genotyping contemporaneously with the experiments. Cells were used within three passages of being thawed. *Mycoplasma* testing was performed using RNA-capture ELISA.

Generation of cell lines expressing doxycycline-inducible shRNA targeting c-Myc

Short hairpin (sh)RNA sequences targeting c-MYC were cloned into the doxycycline-inducible TetOnPLKO lentiviral vector (Addgene; refs. 19, 20) using the following oligonucleotides:

shMYC seq F:
5′-CCGGCCTGAGACAGATCAGCAACAACTCGAGTTGTTGCTGATCTGTCTCAGGTTTTTG

shMYC seq R:
5′-AATTCAAAAACCTGAGACAGATCAGCAACAACTCGAAGTTGTTGCTGATCTGTCTCAGG

The control sequences were:

shCtrl F:
5′-CCGGCCTAAGGTTAAGTCGCCCTCGCTCGAGCGAGGGCGACTTAACCTTAGG

shCtrl R:
5′-AATTCCTAAGGTTAAGTCGCCCTCGCTCGAGCGAGGGCGACTTAACCTTAGG

Lentiviruses were produced by cotransfecting HEK 293T cells with the shRNA plasmid and the packaging plasmids pCMVΔR8.91 (gag-pol) and pMD.G (VSV-G glycoprotein; ref. 21). Supernatants containing lentiviruses were collected 72 hours after transfection, mixed with polybrene (8 μg/mL), and used to infect GB4 cells. Fresh medium containing puromycin (2 μg/mL) was added after 24 hours and cells were selected for at least 48 hours.

c-Myc knockdown

Transduced GB4 cells were grown in 6-well plates to approximately 50% confluency in serum-free medium. Cells were then incubated with doxycycline (10 ng/mL) for 48 hours in serum-free medium, harvested, and protein extracted for Western blot analysis to confirm knockdown of c-Myc and determine the concentrations of LDHA and hexokinase 2 (HK2).

Orthotopic tumor model

Procedures were performed in compliance with project and personal licenses issued under the United Kingdom Animals (Scientific Procedures) Act, 1986 and were approved by the Cancer Research UK, Cambridge Institute Animal Welfare and Ethical Review Body. Tumors were created by intracranial implantation of cells in 6-week-old (200–250g) female rnu/rnu athymic nude rats (Charles River Laboratories; Harlan). Cells, below passage 20, were counted and assessed for viability (Vi-CELL XR, Beckman Coulter) before resuspension in culture media at 2×10^6 cells/μL. Animals were anesthetized by inhalation of 1% to 2% isoflurane (Isoflo, Abbotts Laboratories Ltd.) in O_2 (flow rate 2 L/min). Analgesia, administered subcutaneously (Vetergesic, Alstoe), contained 0.3 mg/mL buprenorphine hydrochloride and 0.135% w/v chlorocresol diluted 1:10 in 0.9% sodium chloride, and 1 mL/kg of subcutaneous Rimadyl LA (Pfizer) containing carpofen (Zoetis; 5 mg/kg diluted 1: 10 in 0.9% sodium chloride). Animals were placed in a stereotactic surgical frame (Kopf) and a 1-mm hole drilled 2 mm anterior and 3 mm lateral to the bregma (right side). Five microliters of the cell suspension was delivered 6 mm intracranially via a 23-gauge full displacement syringe (SGE Analytical Science).

MRI

MR experiments were performed using a 7T spectrometer (Agilent). Animals were anesthetized following inhalation of 1% to 2% isoflurane in O_2 (flow rate 2 L/min) and the core body temperature, breathing, and heart rate were monitored (SA instruments Inc.). Axial ^1H MR (T_2-weighted) images were acquired using a 72-mm inner-diameter ^1H quadrature birdcage coil (RAPID Biomedical GMBH) and a fast spin-echo pulse sequence [TR, 1,500 ms; TE, 40 ms across a matrix of 256×256 data points with a field of view (FOV) of 40×40 mm and 4–8 averages]. Slice thickness was 2 mm and 15 contiguous slices were obtained. Contrast agent-enhanced images were acquired using a T_1-weighted spoiled-gradient-echo sequence prior to and then 90 seconds after injection of 100 μmol/kg Dotarem (Guebert). Images consisted of 5 slices 1.5 mm thick with gaps of 0.3 mm centered on the tumor with TR 43 ms, TE 4.6 ms, 27° flip angle, and four

Published OnlineFirst July 27, 2018; DOI: 10.1158/0008-5472.CAN-18-0759

averages. The field of view was 40 mm × 40 mm with a 256 × 128 data matrix.

Proton magnetic resonance spectroscopy

Lactate spectra were acquired from single 4 × 4 × 4 mm voxels using LASER acquisition (22) and VAPOR water suppression (23) pulse sequences and the 72 mm diameter volume coil for transmit and a quadrature coil placed over the rat's head for receive (Rapid Biomedical). Spectra were acquired with echo times (TE) of 37 and 144 ms and 512 averages, or 1,024 averages for the longer TE. In one tumor, an extra spectrum was acquired with TE 288 ms and 1,024 averages. Water reference spectra were acquired at a TE of 37 ms and using 16 averages. Spectral regions between 1 and 1.6 ppm were least-squares fitted to a model of a lactate–methyl resonance doublet, at all three echo times, and a broad lipid methylene resonance at TE = 37 ms. This fitting was also used to calculate the lactate–methyl resonance T_2. The water T_2 was measured using STEAM localization, using 16 TE values between 0.005 and 0.50 seconds and 16 averages. The lactate–methyl and water T_2s were used to estimate their respective intensities at TE = 0. Assuming a tissue water concentration of 46 mol/L (24), these intensities were used to estimate a lactate concentration. Similar water and lactate spectra were acquired from 6 × 8 × 4 mm voxels in normal brain; 512 averages at TE = 37 ms and 1,024 at TE = 144 s for the lactate spectra and 16 averages at TE = 37 ms for the water spectra. The same T_2 value for lactate and a mean value for the water T_2 in the tumors were used for concentration calculations. Data were processed in MATLAB (Mathworks).

Dynamic nuclear hyperpolarization

[1-^{13}C]pyruvic acid (82 mg) containing 15 mmol/L trityl radical, tris[8-carboxy2,2,6,6-tetra-(hydroxyethyl)-benzo-(1,2-4,50)-bis-(1,3)-dithiole-4-yl]-methyl sodium salt (OXO63; both GE Healthcare) was mixed with 1.5 mmol/L of gadoterate meglumine (Guerbet) and polarized as described previously (25). After dissolution, this gave a 184 mmol/L hyperpolarized [1-^{13}C]pyruvate solution at room temperature with a pH of 7.2 and between 17% and 21% polarization.

^{13}C magnetic resonance spectroscopic imaging

^{13}C spectroscopic images were acquired using a 20-mm diameter transmit/receive surface coil (Varian) inside the 72-mm diameter ^{1}H volume coil and positioned under the supine rat head. T_2-weighted ^{1}H images were used to define a 6-mm slice that incorporated the maximum dimensions of the tumor. A slice-selective shim was then performed. Hyperpolarized [1-^{13}C]pyruvate (10 mL/kg) was injected via a tail vein cannula, which took approximately 10 seconds. Single time point axial ^{13}C chemical shift images were obtained from the 6-mm slice, where image acquisition started 20 seconds after pyruvate injection (TR 30 ms; TE 1.2 ms; FOV 40 × 40 mm; data matrix 32 × 32; sinc excitation pulse with approximate 5° flip angle at 13 mm from the surface coil; spectral width 6,010 Hz; acquisition time 21.3 ms; 128 complex data point pairs; with phase-encoding gradients preceding signal acquisition). Lactate-to-pyruvate ratios were calculated using an in-house MATLAB script. Voxels were included if the signal was 3.5 times the SD determined from 100 voxels in noise regions, and if there was an adjacent voxel that met this criterion. Areas under the peaks were calculated by time-domain fitting of the resonances after spatial Fourier transformation. Animals implanted with GB4 c-myc KD cells were imaged when tumors were >0.1 cm^3. They were then fed a doxycycline diet for 1 week and reimaged (doxycycline diet, 0.2 g/kg food pellet, Harlan D.98186).

Determination of sensitivity to radiotherapy

GB1 and GB4 cell lines were grown in duplicate to 50% confluence and then treated with a single dose (15 Gy) of radiotherapy using a Cs-137 irradiator (IBL 637; CIS Bio International). Cell viability was determined using an automated Trypan blue dye exclusion assay (ViCell) at 1, 3, 5, and 7 days after irradiation.

GB4 control cells, which included nontransduced cells and cells transduced with a lentiviral vector expressing a doxycycline-inducible control shRNA, and GB4 cells expressing a doxycycline-inducible shRNA targeting c-Myc (GB4 c-myc KD) were grown to approximately 50% confluence in serum-free media. They were then treated with either doxycycline (10 ng/mL) alone or doxycycline (10 ng/mL) for 48 hours before treatment with a single dose of 15 Gy and cell viability determined.

GB4 tumor-bearing rats were treated 24 hours after imaging with hyperpolarized [1-^{13}C]pyruvate. Rats were anesthetized using inhalation anesthetic and a lead collimator was used to protect the snout and body. Animals were wrapped in insulating plastic and silver foil to maintain body temperature and Lubrithal (Dechra) was applied for eye protection. For low-dose therapy, temozolomide (100 mg/kg) was dissolved in 1 mL water and administered by oral gavage 1 hour prior to radiotherapy. Radiotherapy (15 Gy) was delivered over 825 seconds using a Cs-137 irradiator (IBL 637; CIS Bio International). The temozolomide dose was split so that 50 mg/kg was given 1 hour prior to the first fraction of radiotherapy (15 Gy) and also 1 hour prior to the second fraction (15 Gy) 72 hours later. A further 10 Gy radiation dose was given 72 hours later giving a total of 40 Gy and 100 mg/kg of temozolomide.

Histopathology and IHC

Brains were excised and immediately placed in 10% formalin (Sigma-Aldrich) for 24 hours, then in 70% ethanol and then sectioned. Hematoxylin and eosin staining (H&E; ST020 Multistainer – Leica Microsystems) was performed on 5-μm sections, which were cut using the surface injection site as a guide for the center of the underlying tumor. Further 10-μm sections were taken for TUNEL staining and IHC. TUNEL was performed using Leica's Polymer Kit (Leica Microsystems) and Promega's DeadEnd Colorimetric TUNEL System (Promega). IHC was performed using Leica's Polymer Refine Kit and human-specific antibodies, specifically Ki67–1:200 dilution (M7240, Dako), Monocarboxylate Transporter (MCT) 1–1:500 dilution (HPA003324, Atlas), MCT 4–1:500 dilution (HPA021451, Atlas), Glial Fibrillary Acid Protein (GFAP)–1:10,000 dilution (Z0334, Dako), c-Myc–1:50 dilution (ab32072, Abcam), and pAKT–1:25 dilution (3787, Cell Signaling Technology). Images were analyzed using Aperio image-viewing software using in-house algorithms.

Published OnlineFirst July 27, 2018; DOI: 10.1158/0008-5472.CAN-18-0759

Western blotting

Protein was extracted from cell and tissue samples in Pierce RIPA buffer, containing protease inhibitor and EDTA (Thermo Fisher Scientific). Cell disruption was performed using either sonication (cell culture; Bioruptor, Diagenode) or via homogenization (tissues; Precellys, Bertin). Proteins were separated using gel electrophoresis in NuPage Bis-Tris precast gels (Thermo Fisher Scientific) and dry-blotted onto polyvinylidene difluoride (PVDF) membranes using an iBlot transfer stack (Thermo Fisher Scientific). Subsequent analysis was performed using a Odyssey Licor near-infrared digital fluorescence imaging system (LI-COR Biotechnology). Samples were analyzed in duplicate or triplicate and data from technical replicates were averaged. Antibodies were used at manufacturer recommended dilutions: c-Myc–Abcam ab32072 1:10,000; pAKT Cell Signaling Technology #9271 1:1,000; HK2–Cell Signaling Technology #2106 1:1,000; LDHA–Cell Signaling Technology #3582 1:1,000.

Whole-exome sequencing

Massively parallel sequencing exome capture was performed using Illumina Nextera Rapid Capture, according to the manufacturer's protocol. Fragment size was confirmed using a Bioanalyser (DNA1000 chip) before precapture pooling and qPCR, using the KAPA Quantification Kit, to confirm DNA concentration. Exome sequencing was performed on an Illumina HiSeq 2500 using v4 chemistry generating 125-bp paired-end reads with dual indexing. Variant calling used a pipeline based on Burrows–Wheeler aligner (BWA). BWA-mem was used for mapping sequencing reads to the human reference genome (GRCh37; ref. 26). The genome analysis toolkit (GATK; version 3.5) was then used to apply local indel realignment and to recalibrate base quality scores (27). Variant calling was carried out jointly using the GATK HaplotypeCaller. Annotation of variants was accomplished using ANNOVAR (28). Oncotator was used for further annotation of candidate variants with cancer relevant annotations (29).

Data availability

Raw data associated with the figures can be accessed at https://doi.org/10.17863/CAM.26052.

Statistical analysis

All statistics were performed using GraphPad Prism (GraphPad Software Inc) and MATLAB (MathWorks).

Results

Patient-derived orthotopic xenografts resemble the human disease

Derivation of the cell lines and the conditions used to culture them have been shown to give GB PDOX models that recapitulate the biology of the tumors from which they were derived (15, 16). The four models studied, originating from 4 individual patients with GB, showed variable growth rates and grew more slowly than the U87 cell line model (Fig. 1A; ref. 30). These models reproduced the morphology of the patient tumors, for example, GB4 had a minimally infiltrative margin compared with GB2, in both the patient tumor and corresponding PDOX (Supplementary Fig. S1A). The models showed high expression of a glial cell marker (GFAP; ref. 31) *in vivo* (Fig. 1B) and a neural stem cell marker (nestin) *in vitro* (Fig. 1C; ref. 15). U87 showed negligible expression of either marker. Exome sequencing showed PTEN frameshift mutations in GB1–3 tumors, which resulted in protein loss (Supplementary Fig. S1B), and in GB4 a frameshift (fs) mutation in PIK3R1 (V73fs), which encodes the regulatory protein p85α and that could lead to activation of PI3K (5, 32; Supplementary Table S1). Consistent with these observations, all the models showed activation of the PI3K/Akt pathway, as indicated by phosphorylation of Akt (pAkt; Supplementary Fig. S1C).

A patient-derived orthotopic xenograft showed increased lactate labeling when compared with normal brain

^{13}C images of non–tumor-bearing animals showed low intensity signals from lactate (Fig. 1D). At 1 month after implantation of GB4 cells, the hyperpolarized [1-^{13}C]lactate/[1-^{13}C]pyruvate signal ratio (LPR) increased significantly in the hemisphere containing injected cells (Fig. 1E) compared with the contralateral hemisphere ($n = 11$, *, $P = 0.02$, paired t test; Fig. 1F). There was no difference in noninjected controls ($n = 6$, $P = 0.9$, paired t test; Fig. 1G). LPR was significantly elevated in the right lower brain quadrant, containing cells, when compared with the left lower quadrant (Fig. 1H; $n = 11$, *, $P = 0.01$, paired t test). There was no difference in the upper right and left quadrants (Fig. 1I). Because the cell injection needle passed through the upper right quadrant, where there was no change in LPR, the increased LPR in the lower right quadrant could not simply be the result of tissue damage. At this stage, no tumor was visible in T_2-weighted ^{1}H MR images of tissue water (Fig. 1J) and there was no signal enhancement in T_1-weighted images following contrast agent injection (Fig. 1K and L).

Tumors derived from different patients showed variable levels of lactate labeling

LPRs measured in tumor-containing regions, identified by hyperintensity on T_2-weighted ^{1}H images, were significantly higher in GB3 and GB4 tumors, whereas GB1 and GB2 tumors showed an LPR similar to normal brain (Fig. 2). Images were acquired when tumors were approximately 0.1 cm^3 or greater. However, GB4 tumors were generally larger than GB1 tumors ($P = 0.03$, GB4 $n = 12$, GB1 $n = 5$, unpaired t test; Supplementary Fig. S1D) and therefore, to eliminate the potential confounding effect of tumor size on LPR, we removed from the analysis all those tumors above a threshold size of 0.35 cm^3. When this was done, there was no longer a significant difference in volume between GB1 and GB4 tumors ($P = 0.3$, GB4 $n = 7$, GB1 $n = 6$, unpaired t test; Supplementary Fig. S1E) but the difference in LPR between GB1 and GB4 was maintained ($P = 0.001$, GB4: $n = 7$, GB1: $n = 6$, unpaired t test; Supplementary Fig. S1F). The variability in labeling in the GB4 model, although large, is comparable with that observed previously in U87 tumors in mice (33).

Lactate labeling correlated with c-Myc expression

Lactate labeling depends upon pyruvate delivery (34), lactate concentration, and the activities of LDH (35) and the MCTs (35, 36). Expression of the MCTs and enzymes in the glycolytic pathway, including LDHA and HK2, is driven by c-Myc (10). The concentrations of c-Myc, LDHA, and HK2 were higher in GB3 and GB4 tumors, which showed high levels of lactate labeling, than in GB1 and GB2 tumors (Fig. 3A–E). This trend, however, was not repeated in cell culture, where GB3 cells showed lower levels of c-Myc than GB2 but comparable levels of LDHA and HK2 (Fig. 3F–H; Supplementary Fig. S2A–F). This

Published OnlineFirst July 27, 2018; DOI: 10.1158/0008-5472.CAN-18-0759

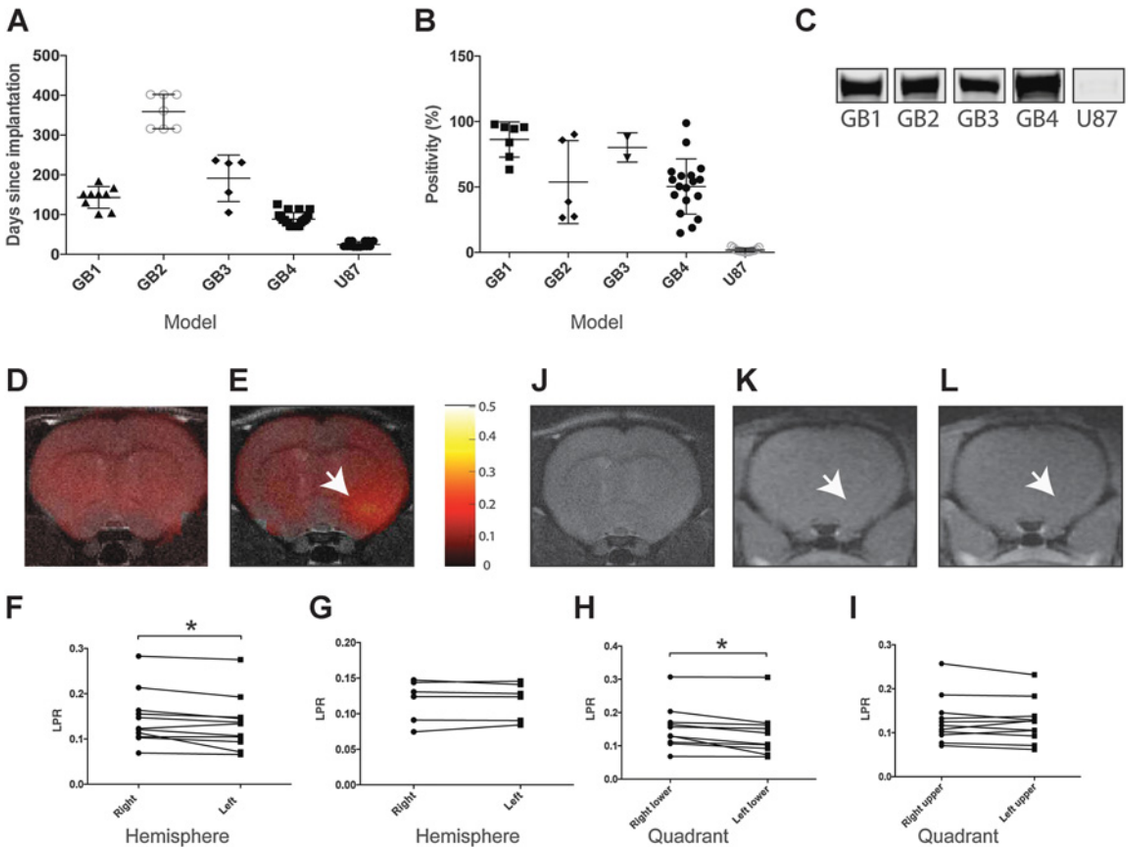

Figure 1.

PDOXs resemble human GB and show increased LPR when compared with normal brain tissue. **A,** Time taken from cell implantation for tumors to reach >0.05 cm^3 (GB1, $n = 9$; GB2, $n = 7$; GB3, $n = 5$; GB4, $n = 21$; U87, $n = 14$; $P < 0.0001$). All of the cell lines showed high levels of tumor initiation and growth following orthotopic cell implantation (GB1, 9 tumors from 9 implantations; GB2, 9/9; GB3, 5/6; GB4, 23/25). **B,** Percentage of cells showing immunostaining for GFAP in the PDOX and U87 tumor models (GB1, $n = 7$; GB2, $n = 5$; GB3, $n = 2$; GB4, $n = 19$; U87, $n = 8$). **C,** Western blot analysis of nestin expression in the indicated cell lines *in vitro*. **D** and **E,** Representative false color images of the LPR superimposed on a T_2-weighted ^{1}H image (grayscale) of a control brain (no implanted tumor cells; **D**) and a brain one month after implantation of GB4 cells (arrow, site of implantation; **E**). Scale bar, LPR. Representative T_2-weighted image (**J**) and T_1-weighted ^{1}H images before (**K**) and after (**I**) contrast agent injection and one month after GB4 cell implantation (arrow, the site of implantation). **F,** LPRs averaged over the hemispheres containing implanted cells (right) and nonimplanted (left) one month after GB4 cell implantation. The ratio was significantly higher in the right hemisphere (*, $P = 0.02$, $n = 11$, paired t test). **G,** LPRs in control brains, which showed no significant difference between the hemispheres ($P = 0.9$, $n = 6$, paired t test). LPRs averaged over the lower (**H**) and upper (**I**) quadrants of the indicated hemispheres one month after GB4 cell implantation in the bottom right brain quadrant. There was a significant increase in the quadrant containing implanted cells (right; *, $P = 0.01$, $n = 11$, paired t test) but no significant difference between the top quadrants ($P = 0.3$, $n = 11$, paired t test).

does not appear to be due to hypoxia because none of the four PDOX models shown here (GB1–GB4) expressed HIF1α *in vivo* (Supplementary Fig. S2G), and only one (GB5), out of the 5 PDOXs studied, expressed HIF1α *in vivo* (Supplementary Fig. S2G). None of the cell lines expressed HIF1α in culture (Supplementary Fig. S2H). Localized proton spectroscopy measurements gave GB4 tumor lactate concentrations of 2 to 8 mmol/L ($n = 4$), as compared with ≤2 mmol/L in normal rat cortex ($n = 2$), consistent with an association between increased HK2 levels and aerobic glycolysis in GB (32). Proton spectra of the brains of two of the four GB4 tumor-bearing animals and spectra from the brains of the two non–tumor-bearing animals are shown in Supplementary Fig. S3. Increased plasma membrane expression of MCTs, a negative prognostic factor in the clinic (37), was observed in tumors with a high LPR (MCT1 in GB3 and GB4 and MCT4 in GB4; Fig. 3I).

Expression of c-Myc (38) and HK2 (39) have been associated with a worse prognosis. We observed a positive correlation between c-Myc expression and LPR ($n = 2$ per GB cohort, $r^2 = 0.83$, **, $P = 0.0017$, linear regression; Fig. 3J), and a correlation, although poorer, between growth rate (Fig. 1A) and c-Myc expression (Fig. 3A, D, and E), with GB1 tumors showing comparable growth rates with GB3 tumors and only slightly lower growth rates than GB4 tumors. However, there was no correlation between tumor growth rate and cell proliferation, as assessed by Ki67 staining, with slower growing GB1 tumors, with low c-Myc expression, showing significantly ($P < 0.0001$) higher levels of Ki67 staining (Supplementary Fig. S2I) than faster growing GB4 tumors, with high c-Myc expression. The reasons for this discrepancy between tumor cell proliferation and tumor growth rate are unclear but cannot be explained by higher rates of cell turnover in GB1 tumors

Published OnlineFirst July 27, 2018; DOI: 10.1158/0008-5472.CAN-18-0759

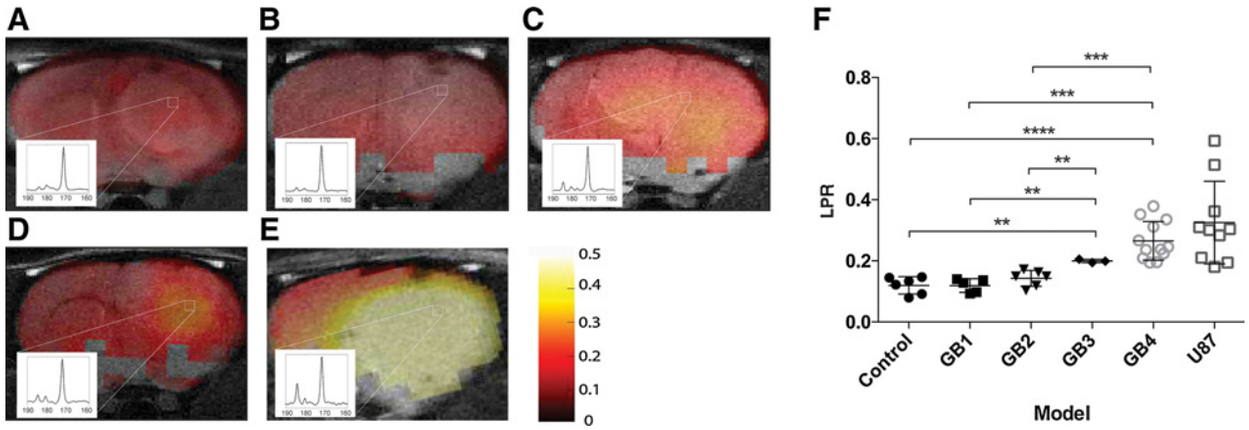

Figure 2.

The different tumor models showed differences in hyperpolarized [1-^{13}C]lactate/[1-^{13}C]pyruvate signal ratios. Representative false color images of the LPR superimposed on T_2-weighted ^{1}H images (grayscale) from animals implanted with GB1 cells (**A**), GB2 cells (**B**), GB3 cells (**C**), GB4 cells (**D**), and U87 cells (**E**). Spectra from representative voxels are also shown. **F,** LPRs in tumors resulting from implantation of the indicated cell lines. Controls were not implanted with cells. (**, $P < 0.009$; ***, $P < 0.0004$; ****, $P < 0.0001$; control, $n = 6$; GB1, $n = 5$; GB2, $n = 9$; GB3, $n = 3$; GB4, $n = 12$; U87, $n = 10$; unpaired t test). Images were acquired at the following times after cell implantation: GB1, 153 days; GB2, 322 days; GB3, 163 days; GB4, 121 days; U87, 27 days.

because there was no difference in the levels of cell death (TUNEL staining) between untreated GB1 and GB4 tumors (Supplementary Fig. S2J).

Inhibition of the PI3K/Akt pathway has been shown previously to decrease GB lactate labeling in animal models injected with hyperpolarized [1-^{13}C]pyruvate (14). However, here there was a negative correlation between the levels of pAKT and LPR ($n = 2$ per GB cohort, $r^2 = 0.76$, $P = 0.0047$; Fig. 3K).

We confirmed that c-Myc–driven expression of LDHA and HK2 was responsible for increased lactate labeling by knocking down c-Myc expression in GB4 cells. Doxycycline treatment of GB4 cells expressing a doxycycline-inducible shRNA targeting c-Myc (GB4 c-Myc KD) substantially decreased c-Myc, LDHA, and HK2 expression (Fig. 4A–C), and in tumors derived from these cells, LPR was decreased 7 days after addition of doxycycline to the diet of tumor-bearing animals (Fig. 4D–F).

Variable lactate labeling in the tumor models reflects intra and intertumoral heterogeneity in patients with GB

Lactate labeling and c-Myc, LDHA, HK2, and MCT expression were reproducible between PDOXs derived from the same patient but different to those derived from other patients. To determine whether this was due to inter or intratumoral heterogeneity, we conducted 5ALA fluorescence-guided multiregion tumor sampling (40) in 4 patients with GB. The levels of c-Myc, HK2, and LDHA varied between 3 to 5 spatially disparate samples (Supplementary Fig. S4A–G), indicating that PDOX heterogeneity reflects patient intra- as well as intertumoral heterogeneity. As in the PDOX models, LDHA and HK2 expression was correlated with c-Myc expression (Supplementary Fig. S4H and S4I; 3–5 regions/tumor, 2 technical replicates per location, $r^2 = 0.30$, $P = 0.036$ and $r^2 = 0.27$, $P = 0.048$, respectively).

Inhibition of c-Myc expression increased radiosensitivity in cultured cells

Expression of HK2 and LDHA have been negatively correlated with radiosensitivity (39, 41), suggesting that metabolic imaging with hyperpolarized [1-^{13}C]pyruvate could be used to target increased radiotherapy dose to areas of radioresistance. We investigated this by comparing the effects of irradiation on GB4 and GB1 cells. Following irradiation, GB4 cells, which have a high LPR *in vivo* (Fig. 2F) and high c-Myc expression *in vitro* and *in vivo* (Fig. 3A and D), showed a greater preservation of viability than GB1 cells (Fig. 4G, $P < 0.0001$), which have a lower LPR *in vivo* (Fig. 2F) and lower levels of c-Myc *in vitro* and *in vivo* (Fig. 3A and D). Doxycycline-induced c-Myc knockdown in GB4 cells resulted in a greater decrease in cell viability following irradiation (Fig. 4H). Control cells (nontransduced cells or cells transduced with a control shRNA) showed no significant difference in viability following irradiation in the presence or absence of doxycycline (Supplementary Fig. S5).

Radiotherapy results in decreased lactate labeling in GB4 tumors

GB4 tumors responded to radiotherapy and temozolomide treatment with a decrease in LPR 72 hours after treatment ($P = 0.038$, $n = 6$, paired t test; Fig. 4I–K). TUNEL staining of excised tumor sections showed that this was accompanied by significant increases in cell death ($P = 0.0089$, $n = 11$ untreated, $n = 8$ treated, unpaired t test; Fig. 4L).

Discussion

Studies in human brain tumors and in patient-derived GB xenografts implanted orthotopically in immunocompromised mice have shown that contrary to expectations, where the tumors were expected to be predominantly glycolytic, there was extensive oxidation of glucose in the tricarboxylic acid (TCA) cycle (42, 43). In these experiments, the patients and mice were infused with ^{13}C-labeled glucose immediately prior to tumor resection and the ^{13}C-labeling patterns in tumor metabolites were analyzed by ^{13}C NMR measurements on tumor extracts. The relatively low levels of lactate labeling

Published OnlineFirst July 27, 2018; DOI: 10.1158/0008-5472.CAN-18-0759

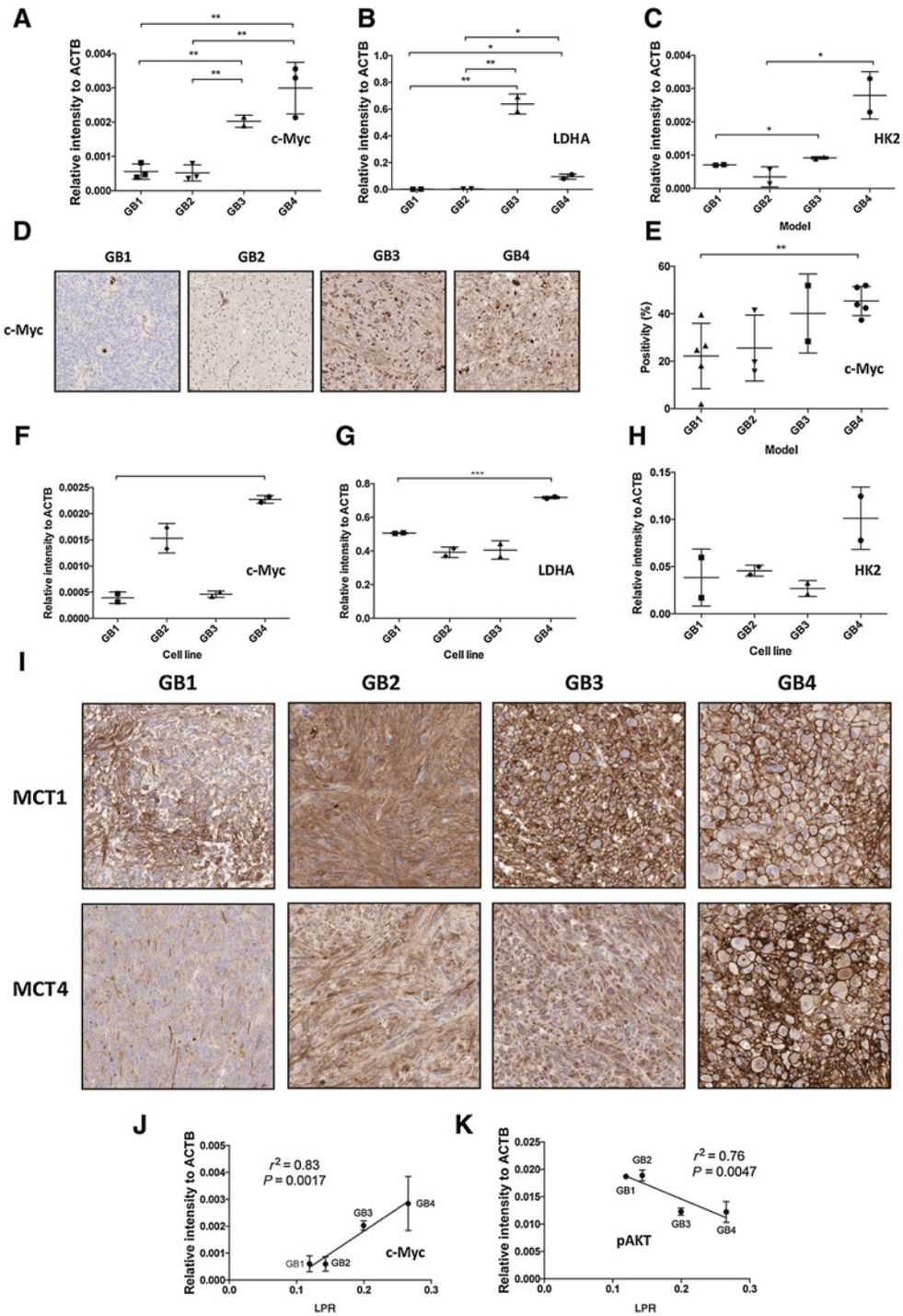

Figure 3.

Expression of c-Myc, LDHA, and HK2 and MCT plasma membrane localization are correlated with the LPR. **A-C,** Western blot analysis of the expression of c-Myc (**A**), LDHA (**B**), and HK2 (**C**) in the indicated tumor models. **D** and **E,** IHC staining of c-Myc in the indicated tumor models (**D**) and quantitative analysis (**E**) of these data (**, $P = 0.009$, $n = 2$–5, unpaired t test). Expression of c-Myc (**F**), LDHA (**G**), and HK2 (**H**) in the corresponding cell lines cultured *in vitro* (*, $P < 0.05$; **, $P < 0.007$; ***, $P < 0.0005$, unpaired t test). For c-Myc, there were three biological replicates and for LDHA and HK2, two and two technical replicates for each sample. Band intensities were normalized to that for β-actin. **I,** IHC analysis of MCT1 and MCT4 expression in the indicated tumor models; plasma membrane localization is evident in GB3 and GB4 tumors. **J** and **K,** Correlations between LPRs measured *in vivo* and c-Myc expression ($r^2 = 0.83$; **, $P = 0.002$, $n = 4$, linear regression; **J**) and phosphorylated Akt (pAKT; $r^2 = 0.76$; **, $P = 0.005$, $n = 4$, linear regression; **K**), determined by Western blotting, in the indicated tumor models.

Published OnlineFirst July 27, 2018; DOI: 10.1158/0008-5472.CAN-18-0759

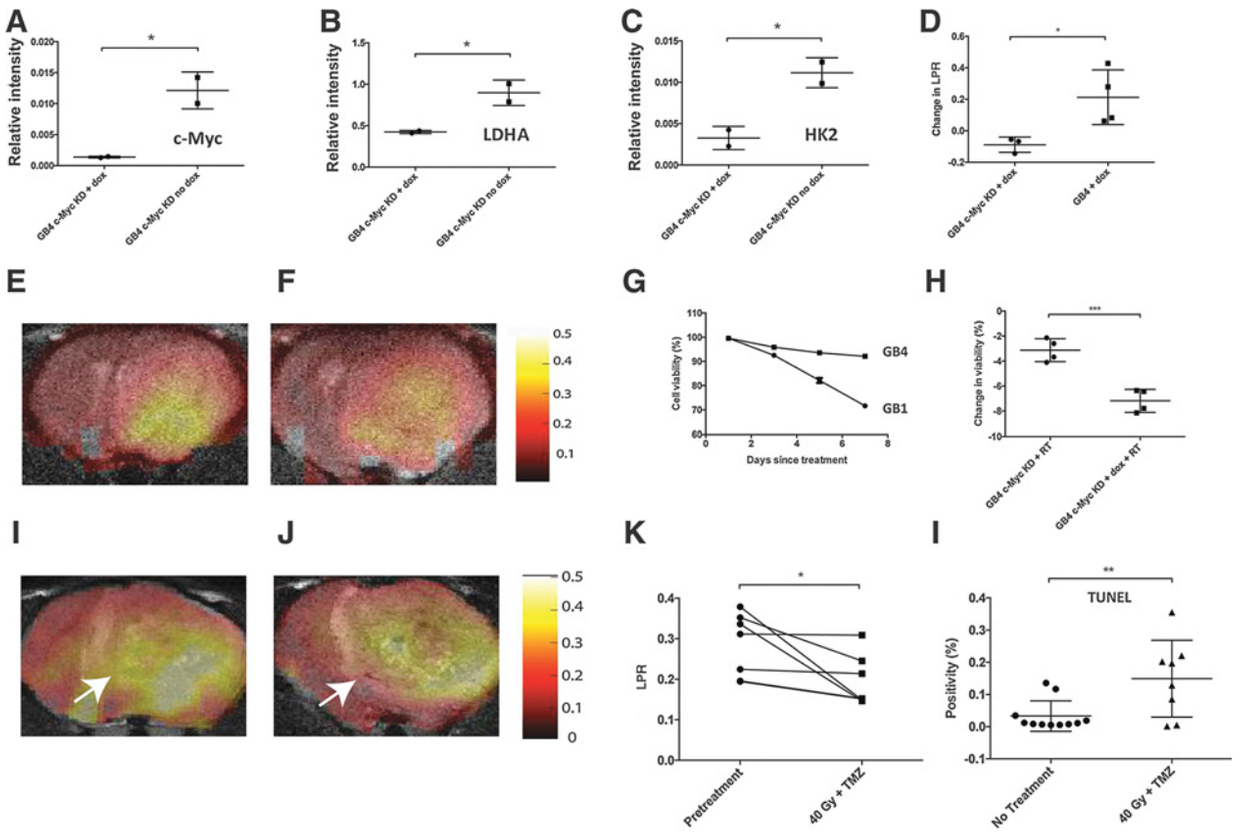

Figure 4.

Inhibition of c-Myc expression decreased the LPR and increased radiosensitivity. **A-C,** Expression of c-Myc, LDHA, and HK2 (normalized to β-actin) 48 hours after addition of doxycycline (dox) to GB4 c-Myc KD cells. There were two biological replicates and two technical replicates per sample (*, $P < 0.05$, unpaired t test). **D,** Change in the LPRs in tumors resulting from orthotopic implantation of GB4 c-Myc KD and GB4 cells one week after addition of doxycycline to the diet (*, $P = 0.035$, $n = 3$, paired t test). LPR images, superimposed on grayscale ^{1}H images, of a GB4 c-Myc KD tumor-bearing rat before (**E**) and after (**F**) addition of doxycycline to the diet. **G,** Response of GB4 and GB1 cells to 15 Gy radiation at day 0 ($P < 0.0001$; two biological replicates; 50 technical replicates; unpaired t test). Viability is shown as the percentage of viable cells determined using an automated Trypan blue dye exclusion assay, as described in the Materials and Methods. **H,** GB4 c-Myc KD cells cultured with doxycycline for 48 hours prior to radiation with 15 Gy showed a significant increase in the loss of cell viability ($P = 0.008$; four biological replicates; 50 technical replicates; unpaired t test). There was no significant difference in the change in viability following irradiation of GB4 cells and GB4 cells expressing a control shRNA between those cells that had previously been incubated with doxycycline and those that had not (Supplementary Fig. S5). LPR images superimposed on ^{1}H images of a GB4 tumor before (**I**) and after (**J**) treatment with temozolomide and 40 Gy of radiation. **K,** LPRs at 72 hours after treatment with temozolomide and 40 Gy of radiation (*, $P = 0.038$, $n = 6$, paired t test). **I,** TUNEL staining of untreated tumors and tumors 72 hours after treatment with temozolomide and 40 Gy of radiation (**, $P < 0.0089$; $n = 11$ untreated; $n = 8$ treated; unpaired t test).

observed in the PDOX models used here, which were similar to those observed in normal brain, are consistent with these previous studies. The much higher levels of lactate labeling observed in the established cell line model used here (U87), and in the GB cell line models used in previous studies with hyperpolarized [1-^{13}C]pyruvate (14), which have been shown to be poor models of human brain tumors (15), reflect presumably their extended lifetime in culture and their very high rates of proliferation rather than being a necessary feature of malignancy. Previous studies with hyperpolarized [1-^{13}C]pyruvate in these cell line models of glioma may, therefore, be overestimating the levels of labeled lactate that are likely to be observed in the clinic. The PDOX models used here, which showed much higher levels of expression of glial (GFAP) and neural stem cell (nestin) markers than the U87 model, are better representative of the human disease.

The patterns of lactate labeling were reproducible between GB PDOXs derived from the same patient but different to those derived from other patients. Multiregion sampling of individual patients with GB showed this likely reflected inter and intratumoral heterogeneity (40). The relatively low levels of lactate labeling in the PDOXs have important implications for translation of this technique to the clinic because they suggest that some tumors, or some regions of tumors, may show lactate labeling that is indistinguishable from labeling in normal brain. However, the observation of increased lactate labeling in brain regions where no tumor was apparent in a T_2-weighted ^{1}H image of tissue morphology also suggests that the technique has the potential to

Published OnlineFirst July 27, 2018; DOI: 10.1158/0008-5472.CAN-18-0759

improve tumor detection, at least in those tumors with higher levels of lactate labeling. A similar observation was made in a clinical study in the prostate, where lactate labeling was observed in tumor tissue that was not detectable in a T_2-weighted ^{1}H image (13).

Although lactate labeling levels were relatively low, we nevertheless observed consistent differences between the different models, which could not be explained by differences in PI3K/Akt pathway activity but which were correlated with the levels of c-Myc, LDHA, HK2, and plasma membrane localization of MCT1 and MCT4. The role of c-Myc in determining tumor lactate labeling, by driving increased expression of HK2 and LDHA, was confirmed by knocking down c-Myc expression in GB4 tumors. This reduced the expression of LDHA and HK2 and decreased lactate labeling. The levels of c-Myc in GB appear to be upregulated by two complementary mechanisms: alternative splicing of deltaMax (44) and mTORC2-dependent phosphorylation and inhibition of HDACs, leading to acetylation and inactivation of FoxO and relief of mir-34c–dependent c-Myc suppression (38). In this latter study, treatment of GB cells with PI3K or Akt inhibitors was shown to elevate c-Myc levels and increase the levels of LDHA and HK2. Consistent with these observations we observed a negative correlation between the levels of pAkt and lactate labeling. The patterns of c-Myc, HK2, and LDHA expression observed in the tumors *in vivo* were not entirely reproduced in the cells cultured *in vitro*. This effect of the tumor microenvironment on gene expression is consistent with a recent RNAi screen of epigenetic modifiers in GB (45), which showed very different results when cells were grown in culture or as orthotopic xenografts.

The expressions of c-Myc (8, 9) and plasma membrane localization of MCT1 and MCT4 (37) have been shown previously to correlate with tumor grade, increased HK2 expression has been correlated with worse overall survival (39), and ^{1}H MRS measurements have demonstrated higher lactate concentrations in grade 3 and 4 tumors (46). Therefore, ^{13}C MRSI measurements of GB lactate labeling could provide prognostic information in the clinic. Moreover, because therapeutic resistance to PI3K or Akt inhibition is mediated by sustained c-Myc activity (38), the technique should also be capable of early detection of drug resistance and response to drugs that modulate c-Myc expression (38, 47). The technique could potentially be used to select patients for metabolic therapies, for example, drugs that target increased c-Myc–driven glycolysis, such as the nicotinamide phosphoribosyltransferase inhibitor, which has demonstrated efficacy in c-Myc–driven GB cells and in patient-derived orthotopic GB xenografts (48).

Detection of response to radiotherapy has been shown previously in a rat cell line glioma model (C6; ref. 25), where response was evident as a decrease in lactate labeling. We have demonstrated here in GB4 tumors, which like C6 tumors show high levels of lactate labeling, that response to concomitant temozolomide and radiation treatment results in decrease in lactate labeling, which was explained by increased levels of cell death. However, detection of response using this technique in those tumors that show much lower levels of lactate labeling may be challenging as the decrease in lactate labeling posttreatment would necessarily be less.

Inhibition of LDHA (41) or HK2 (39) has been shown to sensitize GB cells to radiotherapy and we have shown that c-Myc and glycolytic enzyme expression are correlated with the radioresistance of the cell lines *in vitro*. Therefore, imaging with hyperpolarized [1-^{13}C]pyruvate could potentially be used clinically to target increased radiotherapy dose to radioresistant tumors or specific regions of tumors, that is, regions that display increased lactate labeling. PET with ^{11}C methionine, where the resolution was 4.8 mm, has been used to target radiotherapy in patients with GB (49). Because the resolution in the first clinical studies with hyperpolarized [1-^{13}C]pyruvate in prostate was between 7 and 15 mm (13), the technique may have sufficient spatial resolution to do this.

In summary, increased levels of lactate labeling in GB PDOX models can be explained by increased levels of LDHA, HK2, and plasma membrane MCTs resulting from increased c-Myc expression. With the recent translation of this technique to the clinic, metabolic imaging with hyperpolarized [1-^{13}C]pyruvate could be used clinically for determining disease prognosis, for assessing response to drugs that are effective in reducing the levels of c-Myc, inducing cell death, and for targeting radiation at tumor regions with high c-Myc expression and which are expected to be radioresistant.

Disclosure of Potential Conflicts of Interest

No potential conflicts of interest were disclosed.

Authors' Contributions

Conception and design: R. Mair, A.J. Wright, S. Ros, T.C. Booth, C. Watts, K.M. Brindle

Development of methodology: R. Mair, A.J. Wright, S. Ros, T.C. Booth, K.M. Brindle

Acquisition of data (provided animals, acquired and managed patients, provided facilities, etc.): R. Mair, A.J. Wright, D. Hu, T.C. Booth, F. Kreis, J. Rao, C. Watts

Analysis and interpretation of data (e.g., statistical analysis, biostatistics, computational analysis): R. Mair, A.J. Wright, T.C. Booth, K.M. Brindle

Writing, review, and/or revision of the manuscript: R. Mair, A. Wright, T.C. Booth, C. Watts, K.M. Brindle

Administrative, technical, or material support (i.e., reporting or organizing data, constructing databases): R. Mair, T.C. Booth, C. Watts

Study supervision: K.M. Brindle

Other (provided surgical samples for xenografts): C. Watts

Acknowledgments

The authors acknowledge the support of the Cancer Research UK Cambridge Institute core facilities, in particular the biological resources unit, genomics, bioinformatics, histopathology, and preclinical imaging sections. We would also like to thank Leigh-Anne McDuffus, Jodi Miller, Bev Wilson, Mike Mitchell, Matt Clayton, Ian Hall, Dr. Jane Gray, and Ashley Sawle. The work was supported by a Cancer Research UK Programme grant (17242) and by the CRUK-EPSRC Imaging Centre in Cambridge and Manchester (16465) awarded to K.M. Brindle. F. Kreis was supported by a Marie Curie ITN studentship (EUROPOL) and R. Mair by Addenbrooke's Charitable Trust and a CRUK Cambridge Centre Fellowship.

The costs of publication of this article were defrayed in part by the payment of page charges. This article must therefore be hereby marked *advertisement* in accordance with 18 U.S.C. Section 1734 solely to indicate this fact.

Received March 10, 2018; revised June 6, 2018; accepted July 23, 2018; published first July 27, 2018.

Published OnlineFirst July 27, 2018; DOI: 10.1158/0008-5472.CAN-18-0759

References

1. Ostrom QT, Gittleman H, Fulop J, Liu M, Blanda R, Kromer C, et al. CBTRUS statistical report: primary brain and central nervous system tumors diagnosed in the United States in 2008-2012. Neuro Oncol 2015;17:iv1–iv62.
2. Huse JT, Phillips HS, Brennan CW. Molecular subclassification of diffuse gliomas: seeing order in the chaos. Glia 2011;59:1190–9.
3. Stupp R, Hegi ME, Mason WP, van den Bent MJ, Taphoorn MJ, Janzer RC, et al. Effects of radiotherapy with concomitant and adjuvant temozolomide versus radiotherapy alone on survival in glioblastoma in a randomised phase III study: 5-year analysis of the EORTC-NCIC trial. Lancet Oncol 2009;10:459–66.
4. Wen PY, Kesari S. Malignant gliomas in adults. N Engl J Med 2008;359:492–507.
5. The Cancer Genome Atlas Research Network. Comprehensive genomic characterization defines human glioblastoma genes and core pathways. Nature 2008;455:1061–8.
6. Ward PS, Thompson CB. Metabolic reprogramming: a cancer hallmark even warburg did not anticipate. Cancer Cell 2012;21:297–308.
7. Rodon J, Dienstmann R, Serra V, Tabernero J. Development of PI3K inhibitors: lessons learned from early clinical trials. Nat Rev Clin Oncol 2013;10:143–53.
8. Orian JM, Vasilopoulos K, Yoshida S, Kaye AH, Chow CW, Gonzales MF. Overexpression of multiple oncogenes related to histological grade of astrocytic glioma. Br J Cancer 1992;66:106–12.
9. Herms JW, von Loewenich FD, Behnke J, Markakis E, Kretzschmar HA. c-myc oncogene family expression in glioblastoma and survival. Surg Neurol 1999;51:536–42.
10. Stine ZE, Walton ZE, Altman BJ, Hsieh AL, Dang CV. MYC, metabolism, and cancer. Cancer Discovery 2015;5:1024–39.
11. Ardenkjaer-Larsen JH, Fridlund B, Gram A, Hansson G, Hansson L, Lerche MH, et al. Increase in signal-to-noise ratio of >10,000 times in liquid-state NMR. Proc Natl Acad Sci U S A 2003;100:10158–63.
12. Brindle KM. Imaging metabolism with hyperpolarized (13)C-labeled cell substrates. J Am Chem Soc 2015;137:6418–27.
13. Nelson SJ, Kurhanewicz J, Vigneron DB, Larson PE, Harzstark AL, Ferrone M, et al. Metabolic imaging of patients with prostate cancer using hyperpolarized [1–13C]pyruvate. Sci Transl Med 2013;5:198ra108.
14. Najac C, Ronen SM. MR molecular imaging of brain cancer metabolism using hyperpolarized 13C magnetic resonance spectroscopy. Top Magn Reson Imaging 2016;25:187–96.
15. Lee J, Kotliarova S, Kotliarov Y, Li A, Su Q, Donin NM, et al. Tumor stem cells derived from glioblastomas cultured in bFGF and EGF more closely mirror the phenotype and genotype of primary tumors than do serum-cultured cell lines. Cancer Cell 2006;9:391–403.
16. Wakimoto H, Mohapatra G, Kanai R, Curry WT Jr, Yip S, Nitta M, et al. Maintenance of primary tumor phenotype and genotype in glioblastoma stem cells. Neuro Oncol 2012;14:132–44.
17. Stummer W, Pichlmeier U, Meinel T, Wiestler OD, Zanella F, Reulen HJ. Fluorescence-guided surgery with 5-aminolevulinic acid for resection of malignant glioma: a randomised controlled multicentre phase III trial. Lancet Oncol 2006;7:392–401.
18. Piccirillo SG, Dietz S, Madhu B, Griffiths J, Price SJ, Collins VP, et al. Fluorescence-guided surgical sampling of glioblastoma identifies phenotypically distinct tumour-initiating cell populations in the tumour mass and margin. Br J Cancer 2012;107:462–8.
19. Wiederschain D, Wee S, Chen L, Loo A, Yang G, Huang A, et al. Single-vector inducible lentiviral RNAi system for oncology target validation. Cell Cycle 2009;8:498–504.
20. Wee S, Wiederschain D, Maira S-M, Loo A, Miller C, deBeaumont R, et al. PTEN-deficient cancers depend on PIK3CB. Proc Nat Acad Sci U S A 2008;105:13057–62.
21. Zufferey R, Nagy D, Mandel RJ, Naldini L, Trono D. Multiply attenuated lentiviral vector achieves efficient gene delivery *in vivo*. Nat Biotechnol 1997;15:871–5.
22. Garwood M, DelaBarre L. The return of the frequency sweep: designing adiabatic pulses for contemporary NMR. J Magn Reson 2001;153:155–77.
23. Tkac I, Starcuk Z, Choi IY, Gruetter R. *In vivo* 1H NMR spectroscopy of rat brain at 1 ms echo time. Magn Reson Med 1999;41:649–56.
24. Pfeuffer J, Tkac I, Provencher SW, Gruetter R. Toward an *in vivo* neurochemical profile: quantification of 18 metabolites in short-echo-time (1)H NMR spectra of the rat brain. J Magn Reson 1999;141:104–20.
25. Day SE, Kettunen MI, Cherukuri MK, Mitchell JB, Lizak MJ, Morris HD, et al. Detecting response of rat C6 glioma tumors to radiotherapy using hyperpolarized [1- 13C]pyruvate and 13C magnetic resonance spectroscopic imaging. Magn Reson Med 2011;65:557–63.
26. Li H, Durbin R. Fast and accurate short read alignment with Burrows-Wheeler transform. Bioinformatics 2009;25:1754–60.
27. McKenna A, Hanna M, Banks E, Sivachenko A, Cibulskis K, Kernytsky A, et al. The genome analysis toolkit: a MapReduce framework for analyzing next-generation DNA sequencing data. Genome Research 2010;20:1297–303.
28. Wang K, Li M, Hakonarson H. ANNOVAR: functional annotation of genetic variants from high-throughput sequencing data. Nucleic Acids Res 2010;38:e164.
29. Ramos AH, Lichtenstein L, Gupta M, Lawrence MS, Pugh TJ, Saksena G, et al. Oncotator: cancer variant annotation tool. Hum Mutat 2015;36:E2423–9.
30. Patil V, Pal J, Somasundaram K. Elucidating the cancer-specific genetic alteration spectrum of glioblastoma derived cell lines from whole exome and RNA sequencing. Oncotarget 2015;6:43452–71.
31. Yung WK, Luna M, Borit A. Vimentin and glial fibrillary acidic protein in human brain tumors. J Neurooncol 1985;3:35–8.
32. Mizoguchi M, Nutt CL, Mohapatra G, Louis DN. Genetic alterations of phosphoinositide 3-kinase subunit genes in human glioblastomas. Brain Pathol 2004;14:372–7.
33. Radoul M, Chaumeil MM, Eriksson P, Wang AS, Phillips JJ, Ronen SM. MR studies of glioblastoma models treated with dual PI3K/mTOR inhibitor and temozolomide:metabolic changes are associated with enhanced survival. Mol Cancer Ther 2016;15:1113–22.
34. Reynolds S, Metcalf S, Cochrane EJ, Collins RC, Jones S, Paley MNJ, et al. Direct arterial injection of hyperpolarized 13C-labeled substrates into rat tumors for rapid MR detection of metabolism with minimal substrate dilution. Magn Reson Med 2017;78:2116–26.
35. Witney TH, Kettunen MI, Brindle KM. Kinetic modeling of hyperpolarized 13C label exchange between pyruvate and lactate in tumor cells. J Biol Chem 2011;286:24572–80.
36. Harris T, Eliyahu G, Frydman L, Degani H. Kinetics of hyperpolarized 13C1-pyruvate transport and metabolism in living human breast cancer cells. Proc Natl Acad Sci U S A 2009;106:18131–6.
37. Miranda-Goncalves V, Honavar M, Pinheiro C, Martinho O, Pires MM, Pinheiro C, et al. Monocarboxylate transporters (MCTs) in gliomas: expression and exploitation as therapeutic targets. Neuro Oncol 2013;15:172–88.
38. Masui K, Tanaka K, Akhavan D, Babic I, Gini B, Matsutani T, et al. mTOR complex 2 controls glycolytic metabolism in glioblastoma through FoxO acetylation and upregulation of c-Myc. Cell Metab 2013;18:726–39.
39. Wolf A, Agnihotri S, Micallef J, Mukherjee J, Sabha N, Cairns R, et al. Hexokinase 2 is a key mediator of aerobic glycolysis and promotes tumor growth in human glioblastoma multiforme. J Exp Med 2011;208:313–26.
40. Sottoriva A, Spiteri I, Piccirillo SG, Touloumis A, Collins VP, Marioni JC, et al. Intratumor heterogeneity in human glioblastoma reflects cancer evolutionary dynamics. Proc Natl Acad Sci U S A 2013;110:4009–14.
41. Koukourakis M, Tsolou A, Pouliliou S, Lamprou I, Papadopoulou M, Ilemosoglou M, et al. Blocking LDHA glycolytic pathway sensitizes glioblastoma cells to radiation and temozolomide. Biochem Biophys Res Commun 2017;491:932–8.
42. Maher EA, Marin-Valencia I, Bachoo RM, Mashimo T, Raisanen J, Hatanpaa KJ, et al. Metabolism of [U-(13)C]glucose in human brain tumors *in vivo*. NMR Biomed 2012;25:1234–44.
43. Marin-Valencia I, Yang C, Mashimo T, Cho S, Baek H, Yang XL, et al. Analysis of tumor metabolism reveals mitochondrial glucose oxidation in

Published OnlineFirst July 27, 2018; DOI: 10.1158/0008-5472.CAN-18-0759

genetically diverse human glioblastomas in the mouse brain *in vivo*. Cell Metab 2012;15:827–37.
44. Babic I, Anderson ES, Tanaka K, Guo D, Masui K, Li B, et al. EGFR mutation-induced alternative splicing of Max contributes to growth of glycolytic tumors in brain cancer. Cell Metab 2013;17:1000–8.
45. Miller TE, Liau BB, Wallace LC, Morton AR, Xie Q, Dixit D, et al. Transcription elongation factors represent *in vivo* cancer dependencies in glioblastoma. Nature 2017;547:355–9.
46. Chang SM, Nelson S, Vandenberg S, Cha S, Prados M, Butowski N, et al. Integration of preoperative anatomic and metabolic physiologic imaging of newly diagnosed glioma. J Neurooncol 2009;92:401–15.
47. Annibali D, Whitfield JR, Favuzzi E, Jauset T, Serrano E, Cuartas I, et al. Myc inhibition is effective against glioma and reveals a role for Myc in proficient mitosis. Nat Commun 2014;5:4632.
48. Tateishi K, Iafrate AJ, Ho Q, Curry WT, Batchelor TT, Flaherty KT, et al. Myc-driven glycolysis is a therapeutic target in glioblastoma. Clin Cancer Res 2016;22:4452–65.
49. Miwa K, Matsuo M, Ogawa S-i, Shinoda J, Yokoyama K, Yamada J, et al. Re-irradiation of recurrent glioblastoma multiforme using 11C-methionine PET/CT/MRI image fusion for hypofractionated stereotactic radiotherapy by intensity modulated radiation therapy. Radiat Oncol 2014;9:181.

Published OnlineFirst July 27, 2018; DOI: 10.1158/0008-5472.CAN-18-0759

Cancer Research
The Journal of Cancer Research (1916–1930) | The American Journal of Cancer (1931–1940)

AACR American Association for Cancer Research

Metabolic Imaging Detects Low Levels of Glycolytic Activity That Vary with Levels of c-Myc Expression in Patient-Derived Xenograft Models of Glioblastoma

Richard Mair, Alan J. Wright, Susana Ros, et al.

Cancer Res 2018;78:5408-5418. Published OnlineFirst July 27, 2018.